Macromolecules

pubs.acs.org/Macromolecules Article

Validation and Refinement of Unified Analytic Model for Flexible and Semiflexible Polymer Melt Entanglement

Joseph D. Dietz, Martin Kröger, and Robert S. Hoy*

Cite This: *Macromolecules* 2022, 55, 3613−3626 Read Online

ACCESS | Metrics & More | Article Recommendations

ABSTRACT: We combine molecular dynamics simulations and topological analyses (TA) to validate and refine a recently proposed unified analytic model [Hoy, R. S.; Kröger, M. *Phys. Rev. Lett.* **2020**, *124*, 147801] for the reduced entanglement length, tube diameter, and plateau modulus of polymer melts. While the functional forms of the previously published expressions are insensitive to the choice of the TA method and N_e-estimator, obtaining better statistics and eliminating all known sources of systematic error in the N_e-estimation alters their numerical coefficients. Our revised expressions quantitatively match bead−spring simulation data over the entire range of chain stiffnesses for which systems remain isotropic, semiquantitatively match all available experimental data for flexible, semiflexible, and stiff polymer melts (including new data for conjugated polymers that lie in a previously unpopulated stiffness regime), and outperform previously developed unified scaling theories.

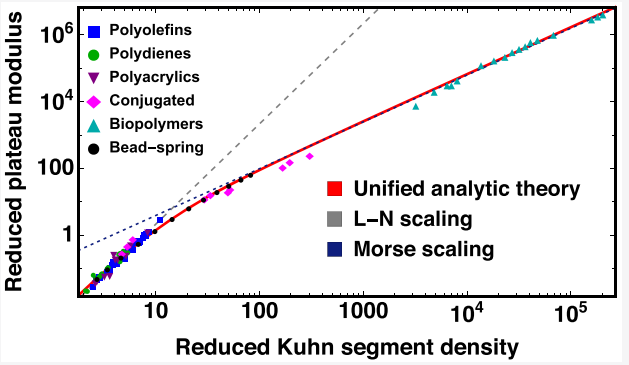

1. INTRODUCTION AND BACKGROUND

Classical tube theories of polymer melt rheology[1−3] describe entanglements collectively as a mean-field phenomenon, where entangled strands of chemical length N_e are confined to soft tube-like regions of diameter a by "topological" constraints arising from chains' mutual uncrossability. However, despite their great successes in predicting the results of rheology experiments,[4−7] they do not predict the values of their key microscopic parameters (e.g., a and the monomeric friction coefficient ζ) from first principles. Instead, such parameters must be entered into the models by hand. First-principles tube theories that *do* predict these parameters have been developed,[8−10] but make simplifying assumptions such as treating entangled segments as rigid rods, and do not have a transparent connection to chain structure on scales below diameter a. Sliplink models offer an alternative first-principles approach to characterizing the rheology of well-entangled systems,[11−13] and accurately predict the results of a wide variety of experiments, but their predictions are usually numerical rather than analytic.

A complete analytic theory of polymer rheology would predict parameters such as N_e and a from microscopic parameters that describe the interchain and intrachain structure of the system, captured, e.g., by the Kuhn length l_K and packing length p, or alternatively by the contour length density $\lambda = \rho l_0$, where ρ is the monomer number density and l_0 is the covalent backbone bond length. An important first step in developing such a theory was Grassley and Edwards' prediction[14] that the reduced plateau modulus Gl_K^3/k_BT (where $G = 4\rho k_BT/5N_e$ is the plateau modulus) should scale as

$$\frac{Gl_K^3}{k_BT} \sim \Lambda^{\mu} \tag{1}$$

where μ is a scaling exponent. The dimensionless quantity Λ can be written in at least four mathematically equivalent (and thus interchangeable) forms via the identity

$$\Lambda \equiv \lambda l_K^2 \equiv \frac{l_K}{p} = \rho_K l_K^3 = \frac{l_K^3}{v_K} \tag{2}$$

where ρ_K is the number density of Kuhn segments, v_K is the volume of a Kuhn segment, and $p = (\rho l_0 l_K)^{-1}$ is the packing length implicitly defined by eq 2.[15] Roughly speaking, Λ is small for "fat, flexible" chains in systems with $l_K \ll a$ and large for "skinny, stiff" chains in systems with $l_K \gg a$. Typical values range from 1−10 for commodity-polymer melts to 10^3−10^5 for F-actin solutions.[15−19]

Received: December 21, 2021
Revised: March 23, 2022
Published: April 20, 2022

Multiplying the inverse of eq 1 by Λ yields the scaling of the reduced entanglement length

$$\frac{L_e}{l_K} \sim \Lambda^{1-\mu} \tag{3}$$

where $L_e = N_e l_0$ is the contour length of entangled strands. Assuming $a^2 = L_e l_K$ and taking the square root of eq 3 yields the scaling of the reduced tube diameter

$$\frac{a}{l_K} \sim \Lambda^{(1-\mu)/2} \tag{4}$$

However, while Graessley and Edwards showed that the available experimental data were consistent with $\mu \simeq 2.3$ and $\mu \simeq 2$ for semidilute and concentrated solutions,[14] their theoretical arguments did not *predict* the value of μ. Doing so requires introducing a geometrically and/or physically motivated ansatz for what constitutes an entanglement.

Four successful "traditional" scaling theories for polymer entanglement[20−25] remain in common use. Each of these theories is based on a distinct ansatz. Lin−Noolandi scaling[20,21] assumes that there are a constant, chemistry-independent number of entangled strands per cubic tube diameter and predicts $\mu = 3$. Combined with the packing model,[15] this picture accurately predicts G for flexible polymers, i.e., for most synthetic commodity polymers.[15−17] Morse scaling[22] views entanglement as a binary-contact event between a transversely thermally fluctuating chain segment of length L_e and an obliquely oriented chain segment within its vicinity and predicts $\mu = 7/5$ or $\mu = 4/3$ depending on the approximations employed.[a] This picture accurately predicts the $G_N^0 \sim \rho^{7/5}$ scaling observed in solutions of stiff biopolymers such as F-actin.[18,19] Edwards−de Gennes scaling[23,24] assumes that there are a constant number of binary interchain contacts per entanglement and predicts $\mu = 2$. This picture accurately predicts the concentration dependence of G_N^0 in concentrated flexible-polymer solutions, i.e., $G_N^0 \sim \rho^2$.[14,26,27] Finally, Colby−Rubinstein scaling[25] assumes that there are a constant number of binary contacts per cubic tube diameter and predicts $\mu = 7/3$, which correctly describes the $G_N^0 \sim \rho^{7/3}$ scaling found in semidilute flexible-polymer solutions.[14,26,27]

The ansatzes used to derive the four theories are—at least apparently—mutually incompatible. Moreover, since each theory is well supported by experiments in the range of Λ it was designed to treat,[15−19,26,27] none of them can be correct for all Λ. Developing unified analytic expressions for entanglement-related quantities that are accurate for arbitrary Λ allows one to predict rheological properties from microscopic parameters that are readily experimentally measurable, enabling more efficient design of polymers for various specific applications.[28] Such relationships are expected to hold irrespective of whether linear-viscoelastic stresses are dominated by entropic or energetic contributions, provided systems remain isotropic and chains are sufficiently well entangled.[28−31] For example, Morse scaling[22] arises from assuming that curvature elasticity rather than entropic elasticity is responsible for the value of the low-frequency plateau modulus $G \sim \lambda/L_e$, but this is also captured by eqs 1−3.

As a result, several groups have attempted to unify the traditional scaling theories. Uchida, Grest, and Everaers began these efforts by developing[32] crossover expressions for L_e/l_K and a/l_K:

$$\frac{L_e}{l_K} \approx (c_\xi \Lambda)^{-2/5} + (c_\xi \Lambda)^{-2} \tag{5}$$

and

$$\frac{G l_K^3}{k_B T} = \frac{c_G c_\xi^{2/5} \Lambda^{7/5}}{[1 + (c_\xi \Lambda)^{-2/5} + (c_\xi \Lambda)^{-2}]^{4/5}} \tag{6}$$

involving two numerical coefficients c_ξ and c_G. These expressions capture the crossover from the $\mu \simeq 3$ scaling of dense flexible-chain melts to the $\mu \simeq 7/5$ scaling of semidilute stiff-chain solutions and agree reasonably well with data for systems with a very wide range of Λ.[32] However, since their theory does not include contributions associated with the binary-contact ansatz, it neglects $\mu = 2$ scaling. Nor does it capture the crossover to $\mu = 7/3$ scaling as the polymer volume fraction (and thus ρ) decreases.

More recently, two simultaneous independent efforts have attempted further unification. Milner proposed[33] a unified geometrical framework wherein the degree of entanglement is predicted by binary-contact probabilities between the structures that are responsible for entanglement. For dense flexible-chain melts with $l_K \ll a$, identifying these structures as packing blobs of diameter p predicts Lin−Noolandi ($\mu = 3$) scaling. As chain stiffness increases into the semiflexible ($l_K \simeq a$) regime, p drops below the chain diameter d and (in Milner's picture) becomes irrelevant. When this happens, the structures controlling entanglement switch from packing blobs to Kuhn segments. Using the fact that binary contact between these segments occurs as their transverse motion sweeps out an area of size l_K^2 predicts Edwards−de Gennes ($\mu = 2$) scaling. For stiff polymers with $l_K \gg a$, using the fact that the probability of observing one "near miss" binary contact event between two entangled strands scales with the intercept area aL_e times the contour length density λ predicts Morse ($\mu = 7/5$) scaling. Semidilute solutions of both flexible and semiflexible polymers are treated by identifying the entangling structures as correlation blobs of size ξ, which predicts Colby−Rubinstein scaling ($\mu = 7/3$) for flexible chains and a new power law ($\mu = 9/4$) for semiflexible chains. Thus, ref 33 describes all known scalings of Gl_K^3/k_BT within a single picture. It does not, however, treat any of the (potentially broad) crossovers between regimes with different μ.

Two of us proposed[34] analytic expressions for L_e/l_K, a/l_K, and Gl_K^3/k_BT that unify three of the four traditional scaling regimes and treat the crossovers between them. Specifically, we proposed

$$\frac{L_e}{l_K} = \frac{N_e}{C_\infty} = c_1 \Lambda^{-2} + c_2 \Lambda^{-1} + c_3 \Lambda^{-\epsilon} \tag{7}$$

$$\frac{a}{l_K} = \sqrt{c_1 \Lambda^{-2} + c_2 \Lambda^{-1} + c_3 \Lambda^{-\epsilon}} \tag{8}$$

and

$$\frac{G l_K^3}{k_B T} = \frac{4}{5}[c_1 \Lambda^{-3} + c_2 \Lambda^{-2} + c_3 \Lambda^{-(1+\epsilon)}]^{-1} \tag{9}$$

where the chemistry-independent prefactors c_1, c_2, and c_3 weigh the contributions[b] from flexible-, semiflexible-, and stiff-chain

https://doi.org/10.1021/acs.macromol.1c02597
Macromolecules 2022, 55, 3613−3626

entanglement, and $\varepsilon = 1/3$ was chosen to correspond to the $\mu = 1 + \varepsilon = 4/3$ version of Morse's theory. Equations 7−9 reduce to the Graessley−Edwards predictions $L_e/l_K \sim \Lambda^{1-\mu}$, $a/l_K \sim \Lambda^{(1-\mu)/2}$, and $Gl_K^3/k_BT \sim \Lambda^{\mu}$ when one of their c_i-terms is large compared to the others. In other words, they reduce to Lin−Noolandi, Edwards−de Gennes, and Morse scaling in the limits these theories were designed to treat.

Equations 7−9 agree quantitatively with simulation data[34] for L_e/l_K, a/l_K, and Gl_K^3/k_BT for bead−spring polymer melts of two different densities and chain stiffnesses spanning the entire range for which systems remain isotropic. The values $c_1 = \alpha(\rho l_0^3)^2 \simeq 97.5$, $c_2 = \beta(\rho l_0^3) \simeq 17.9$, and $c_3 = \gamma(\rho l_0^3)^{\epsilon} \simeq 1.34$ were obtained by fitting the higher-density melts' topological entanglement lengths (obtained via Z1 analysis[35]) to

$$N_e(C_\infty) = \alpha C_\infty^{-3} + \beta C_\infty^{-1} + \gamma C_\infty^{1-2\epsilon} \tag{10}$$

where $C_\infty = l_K/l_0$ is Flory's characteristic ratio.[36] Here the powers of $(\rho l_0^3)^{\mu-1}$ and $C_\infty^{3-2\mu}$ arise from the identity $\Lambda^\mu \equiv (\rho l_0^3)^\mu C_\infty^{2\mu}$; determining the $\{c_i\}$ in this fashion converts a ρ-dependent expression (eq 10) into a ρ-independent one (eq 7) that correctly predicted L_e/l_K for both densities.[34] The crossover regimes where two of the three terms in eqs 7−10 are comparable in magnitude were broad, suggesting that the geometrical cartoons underlying Lin−Noolandi, Edwards−de Gennes, and Morse scaling are, after all, *cartoons* that oversimplify how entanglement occurs in real polymer melts. However, ref 34 did not attempt either to account for the fact that TA results can be highly sensitive to both the TA method employed and the mathematical formula used to estimate N_e[37,38] or to compare eqs 7−9 to experimental data. Nor did it attempt to treat the crossovers to $\mu = 7/3$ or $\mu = 9/4$ scaling that occur as ρ decreases.

In this paper, we resolve the first two of these three open questions by performing molecular dynamics (MD) simulations and topological analyses on a much larger ensemble of bead−spring melts composed of much longer chains. We find that the functional forms of eqs 7−9 are robust against changing the TA method and N_e-estimator, provided that pathological estimators are avoided. Then we show that obtaining better statistical sampling and eliminating all known sources of systematic error in the N_e estimation both alters their c-coefficients and *may* allow them to be simplified by removing the $\mu = 2$ scaling terms, i.e., by setting $c_2 = 0$. Finally we show that the revised expressions quantitatively match simulation data for L_e/l_K and Gl_K^3/k_BT over the entire range of Λ for which dense bead−spring melts remain isotropic, semiquantitatively match all available experimental data for flexible, semiflexible, and stiff polymer melts (including new data for conjugate polymers that lie in a previously unpopulated Λ-regime[28]), and outperform all previously proposed expressions.

2. MODEL AND METHODS

2.1. Molecular Dynamics Simulations. Our studies employ the semiflexible variant of the standard Kremer−Grest model.[39,40] All monomers interact via the Weeks−Chandler−Anderson potential[41]

$$U_{\mathrm{LJ}}(r) = 4\epsilon\left[\left(\frac{\sigma}{r}\right)^{12} - \left(\frac{\sigma}{r}\right)^{6}\right], \quad r \le r_c \tag{11}$$

where ϵ and σ are characteristic energy and length scales, r is the intermonomer distance, and $r_c = 2^{1/6}\sigma$ is the cutoff radius. Covalent bonds are modeled by using the finitely extensible nonlinear elastic (FENE) potential[42]

$$U_{\mathrm{FENE}}(l) = -\frac{k_{\mathrm{FENE}}R_0^2}{2}\ln[1 - (l/R_0)^2] \tag{12}$$

for bonds of length l, where $k_{\mathrm{FENE}} = 30\epsilon\sigma^{-2}$ and $R_0 = 1.5\sigma$. Angular interactions between three consecutive monomers along chain backbones are modeled by using the bending potential

$$U_{\mathrm{ang}}(\theta) = \kappa(1 - \cos\theta) \tag{13}$$

where $\theta = \cos^{-1}(\hat{\mathbf{b}}_i \cdot \hat{\mathbf{b}}_{i+1})$ is the angle between consecutive bond vectors $\mathbf{b}_i$ and $\mathbf{b}_{i+1}$. This model for semiflexible polymers, used for decades,[43,44] was shown recently by Svaneborg, Everaers, and colleagues to accurately capture the dynamics of a wide variety of commodity polymer melts when ϵ, σ, and κ are mapped to SI units.[38,45]

We examine systems with $0.0 \le \kappa/\epsilon \le 5.5$; these span the full range of chain stiffness for which melts remain isotropic.[40] All our simulated systems are fully equilibrated melts consisting of N_{ch} chains of N monomers, with $N_{\mathrm{ch}}N \simeq 4 \times 10^5$ and six different N in the range $100 \le N \le 800$. Systems were prepared and equilibrated as described in ref 46; all MD simulations were performed by using LAMMPS.[47] All results presented below are averages over 10 independently prepared systems (for each κ) and 21 snapshots for each system, separated in time by the entanglement time $\tau_e(\kappa)$ (Appendix B). At the monomer number density ($\rho = 0.85\sigma^{-3}$) and temperature ($k_BT = \epsilon$) employed in this study, the polymers' Kuhn lengths are well described by[46]

$$\frac{l_K}{l_0} \approx \frac{2\kappa/\epsilon + \exp(-2\kappa/\epsilon) - 1}{1 - \exp(-2\kappa/\epsilon)(2\kappa/\epsilon + 1)} + 0.364 \times \left\{\tanh\left[0.241\left(\frac{\kappa}{\epsilon}\right)^2 - 1.73\frac{\kappa}{\epsilon} + 2.08\right] + 1\right\} \tag{14}$$

These values correspond to the range $2.7 \le \Lambda \le 82$ (Table 1), which (as we will show below) is more than sufficient to accurately capture the crossovers between the various scaling regimes.

2.2. Topological Analyses. We characterize the entanglement of these systems using two different topological analysis (TA) methods: primitive path analysis (PPA)[48] and Z1+. Both work by fixing chain ends in space, setting all particles' velocities to zero, and then performing a minimization process that maintains interchain uncrossability and reduces melts to their corresponding primitive path network.

In PPA, several changes are made to the interaction potentials. No attempt is made to preserve self-entanglements since their number is very small for the dense melts considered here.[49] Intrachain excluded-volume (i.e., Lennard-Jones) interactions are deactivated, allowing chains to reduce their contour length. Covalent bonds are strengthened by setting $k_{\mathrm{FENE}} = 100\epsilon\sigma^{-2}$, and the angular potential is deactivated.[49] The system is then coupled to a heat bath at $T = 10^{-3}\epsilon/k_B$ to suppress thermal fluctuations, and Newton's equations of

https://doi.org/10.1021/acs.macromol.1c02597
Macromolecules 2022, 55, 3613−3626

Table 1. Properties Characterizing the Semiflexible Kremer–Grest Melts Studied in This Work[a]

κ [ϵ]	C_∞	l_K[σ]	p [σ]	v_K [σ^3]	ρ_K [σ^{-3}]	Λ	Z_{max}	N_e^{topo}	N_e^{rheo}	N_{eK}	a [σ]	a/p	$\Lambda^{1/2}a$	Gl_k^3/k_BT
0.0	1.89	1.82	0.67	2.22	0.45	2.7	19.7	37.6	80.5	42.7	11.89	17.75	10.77	0.05
0.5	2.12	2.04	0.60	2.49	0.40	3.4	27.0	28.4	58.9	27.8	10.77	18.04	9.75	0.10
1.0	2.46	2.37	0.51	2.90	0.35	4.6	39.6	20.6	41.1	16.7	9.69	18.85	8.77	0.22
1.5	2.98	2.88	0.42	3.51	0.28	6.8	25.7	14.8	28.4	9.5	8.88	20.92	8.04	0.57
2.0	3.59	3.46	0.35	4.22	0.24	9.8	35.4	10.9	20.5	5.7	8.26	23.38	7.47	1.37
2.5	4.34	4.18	0.29	5.11	0.20	14.3	45.8	8.54	15.8	3.6	7.99	27.37	7.23	3.15
3.0	5.22	5.03	0.24	6.14	0.16	20.7	55.4	7.11	13.2	2.5	8.00	32.98	7.24	6.56
3.5	6.15	5.93	0.21	7.24	0.14	28.8	63.0	6.28	11.8	1.9	8.20	39.83	7.42	12.03
4.0	7.14	6.88	0.18	8.40	0.12	38.8	68.4	5.81	11.0	1.5	8.54	48.14	7.73	20.11
4.5	8.14	7.84	0.16	9.57	0.10	50.3	72.2	5.55	10.6	1.3	8.95	57.45	8.10	30.92
5.0	9.31	8.97	0.14	11.0	0.09	66.0	74.3	5.40	10.4	1.1	9.47	69.64	8.57	47.37
5.5	10.37	9.99	0.12	12.2	0.08	81.8	75.0	5.31	10.3	1.0	9.94	81.34	9.00	66.10

[a]All systems have bead number density $\rho = 0.85\sigma^{-3}$. The bond length l_0 is basically identical for all systems, weakly decreasing from 0.9648 ($\kappa = 0\epsilon$) to 0.9637 ($\kappa = 5.5\epsilon$). Hence, $\lambda = \rho l_0 \approx 0.82$ is also approximately constant. Quantities listed here include the chain stiffness κ, characteristic ratio C_∞, Kuhn length l_K, packing length p, Kuhn monomer volume v_K, number density of Kuhn monomers ρ_K, dimensionless Λ (eq 2), mean number of kinks $Z_{max} = \langle Z \rangle (N_{max})$ in our longest simulated chains ($N_{max} = 800$ for $\kappa \leq 1.0\epsilon$ and $N_{max} = 400$ for $\kappa > 1.0\epsilon$), estimated topological and rheological entanglement lengths N_e^{topo} and N_e^{rheo}, and finally the number of Kuhn segments per entanglement N_{eK}, tube diameter a, reduced tube diameters a/p and $\Lambda^{1/2}a$, and reduced plateau modulus Gl_K^3/k_BT obtained using N_e^{rheo}.

motion are integrated in the presence of a thermostat until the chains have locally minimized their total (pair + bond) energy.[c] Chains usually do not disentangle on their way toward such a minimum because of the corrugated surface of the bead–spring chains. This process typically requires $\sim 10^3 \tau_{LJ}$ to converge to a final mean contour length L_{pp} per chain.

Z1+ ignores bead volume and reduces chains to their primitive paths (PPs) without disentangling the chains by performing various geometrical operations, reducing chains to a series of line segments ending in "kinks" that correspond to contacts between PPs. It uses a completely different methodology than Z1, which makes it computationally faster than Z1 for large systems. Specifically, Z1+ recognizes kinks by applying an angle criterion and checking for the existence of pairs of chains that give rise to each of the nonvanishing angles on the shortest path, and thus provides not only L_{pp}, but also a number of kinks Z for each chain, as well as the bead IDs corresponding to binary entanglements.

The topological entanglement length (N_e^{topo}, the *step* length of the PPs[48,50]) is given by[37]

$$N_e^{topo} = \lim_{N\to\infty} \mathcal{N}_e^{M\text{-kink}} \tag{15}$$

with the N-dependent estimator

$$\frac{1}{\mathcal{N}_e^{M\text{-kink}}} = \frac{d\langle Z \rangle}{dN} \tag{16}$$

where $\langle Z \rangle$ is the average number of kinks per chain. Finite-N effects can be identified and (ideally) eliminated by using this estimator with information from a series of chain lengths. Z1 and Z1+ give nearly identical results for the PP contour lengths, but different results for $\langle Z \rangle (N)$. Specifically, we have found that Z1+ gives faster convergence of $\mathcal{N}_e^{M\text{-kink}}$ with increasing N. This feature, along with other considerations related to kink definitions and computational efficiency,[d] will be discussed in an upcoming publication.

Both PPA and Z1+ reduce the average chain contour length from its initial value $L = (N-1)l_0$ [where $l_0 = 0.964\sigma - 0.967\sigma$ is the equilibrium FENE bond length] to L_{pp}. The number of Kuhn segments per entanglement strand, $N_{eK} = N_e/C_\infty \equiv L_e/l_K$, can be estimated by using the reinterpreted wormlike chain formula recently proposed by Svaneborg and Everaers:[38]

$$\left(\frac{L_{pp}}{L}\right)^2 = \frac{2\mathcal{N}_{eK} + \exp(-2\mathcal{N}_{eK}) - 1}{2\mathcal{N}_{eK}^2} \tag{17}$$

where $\mathcal{N}_{eK}$ is determined from L_{pp} as a function of N, and $N_{eK} = \lim_{N\to\infty} \mathcal{N}_{eK}$. Note in passing that eq 17 can be derived from the "M-coil" N_e-estimator[37] upon assuming $N_e \gg 1$, $L_{pp} \propto N$, and wormlike chain statistics for the end-to-end distance. Then the numerically estimated rheological entanglement length (N_e^{rheo}, the *Kuhn* length of the PPs[48,50]) is

$$N_e^{rheo} \equiv \lim_{N\to\infty} \mathcal{N}_e^{SE} = N_{eK} l_K / l_0 \tag{18}$$

Note that in general, neither PPA nor Z1+ produces unique results for a given system; they respectively tend to sample a range of low-lying energy minima and shortest-path minima rather than finding a global minimum. In many cases the global minimum is degenerate. Fortunately, this does not seem to produce large changes in estimated N_e values, especially after ensemble averaging as we have done here.

It is well established that topological analysis results are dependent on both the TA method and the postprocessing employed.[35,37,49,51] For example, N_e^{topo} values obtained by enumerating $\langle Z \rangle$ are consistently well below rheological estimates N_e^{rheo} obtained from the chain statistics of PPs if random walk statistics are assumed for the PPs (Table 1). The accepted interpretation of this discrepancy is that primitive paths have a finite persistence length.[48] Everaers used[50] a binary-contact model to postulate $N_e^{rheo}/N_e^{topo} = 2$, and the same ratio is predicted by slip-link models,[52−54] but the N_e^{rheo}/N_e^{topo} obtained from molecular simulations is expected to vary with the employed Z-algorithm and kink definition. Substantial differences between N_e values obtained by using estimators of the same kind also occur. Reasons for these include primitive chain thickness,[51,55] differences in the criteria

https://doi.org/10.1021/acs.macromol.1c02597
Macromolecules 2022, 55, 3613−3626

used to identify contacts between PPs,[35,51] energy minimization versus contour length minimization,[56] and the fact that employing PPA can result in loosening of entanglements. The latter does not occur in Z1+ or in the alternative TA method CReTA.[51] As we will show below, because of the neglected bead volume, L_{pp} values obtained by using Z1+ tend to be smaller than those obtained by using PPA, leading to substantially larger predicted N_{eK}.

Another important consideration is the mathematical pathologies present in many N_e-estimators. Key among the latter are systematic errors associated with finite-N effects and the non-Gaussian statistics of primitive paths.[37,38] Accurately estimating N_e requires correcting errors of this type. For example, although eq 17 removes the faulty assumption—present in all previously developed estimators for N_e^{rheo} with the exception of the M-coil estimator described in ref 37—that primitive paths are random-walk-like between consecutive entanglements, it suffers from a systematic $O(N^{-1})$ error stemming from its improper treatment of chain ends. Specifically, it incorrectly predicts that $\mathcal{N}_{eK} = 0$ for unentangled chains with $L_{pp} = L$. Fortunately the associated error can be removed by extrapolating results to the $N \to \infty$ limit.

In the following section, we will compare results for N_e^{rheo} and N_e^{topo} to each other and to those for other previously developed N_e-estimators and discuss the implications of any differences between them, while devoting great care to eliminating all systematic errors. Our ultimate aim will be to obtain versions of eqs 7−9 that best match experimental data, *using only bead−spring data.*

3. RESULTS AND DISCUSSION

Robustly testing the three relationships (7)−(9) requires answering two prerequisite questions. First, how does one optimally determine the dimensionless variables N_e and Λ? Second, how does one identify the optimal fitting coefficients c_1, c_2, and c_3? We will focus on answering these questions in the following sections. With answers at hand, we will be in a position to provide analytic expressions that quantitatively capture our coarse-grained simulation results. Critically, the resulting expressions also quantitatively capture the available experimental data for polymer melts and can thus be assumed to predict results from atomistic simulation.

3.1. How to Obtain N_e. As discussed above, a key quantity employed by N_e-estimators such as eq 17 is the average primitive path length L_{pp}. We begin this section by illustrating a nontrivial coupling between the TA method and $L_{pp}(\kappa)$. Figure 1 contrasts the $L_{pp}(\kappa)$ for chain lengths $100 \le N \le 800$ obtained via PPA and Z1+. As shown in Figure 1a, PPA values of L_{pp} are systematically larger. This is expected since PPA yields bead−spring-based PPs that are the same thickness as the polymer chains, while Z1+ yields zero thickness PPs mathematically represented as sequences of line segments.[35] Geometrical intuition suggests that PPA values of L_{pp} should be larger by a factor $O[\sigma/(N_e l_0)] = O[\sigma/L_e]$. Data for $L_{pp}^{PPA}/L_{pp}^{Z1+}$ (Figure 1b) are broadly consistent with this intuition. For example, flexible chains in the large-N limit have $1.0 \le L_{pp}^{PPA}/L_{pp}^{Z1+} \le 1.01$, which is consistent with their $N_e \simeq 80$, while semiflexible chains with $\kappa \gtrsim 3\epsilon$ have $L_{pp}^{PPA}/L_{pp}^{Z1+} \simeq 1.1$, which is consistent with their $N_e \simeq 10$ (eq 20). Figure 1b also illustrates a nonmonotonicity in $L_{pp}^{PPA}/L_{pp}^{Z1+}$—it is maximized for $\kappa \simeq 3\epsilon$ and afterward decreases with increasing κ—that is not matched by any corresponding nonmonotonicity in N_e. The origin of this discrepancy is obscure; isolating it would require comparing to results for other polymer models, which we do not attempt here. Critically, however, the nonunity and nonmonotonicity of $L_{pp}^{PPA}(\kappa)/L_{pp}^{Z1+}(\kappa)$ indicate that the c-coefficients in eqs 7−9 (obtained from the $N_e(\kappa)$ values calculated via eq 17) have a nontrivial TA-method dependence. Because it is not *a priori* clear which TA method yields $L_{pp}(\kappa)$ and $N_e(\kappa)$ that better predict the rheology of real polymer melts, we will attempt to resolve this issue by using other criteria, as detailed below.

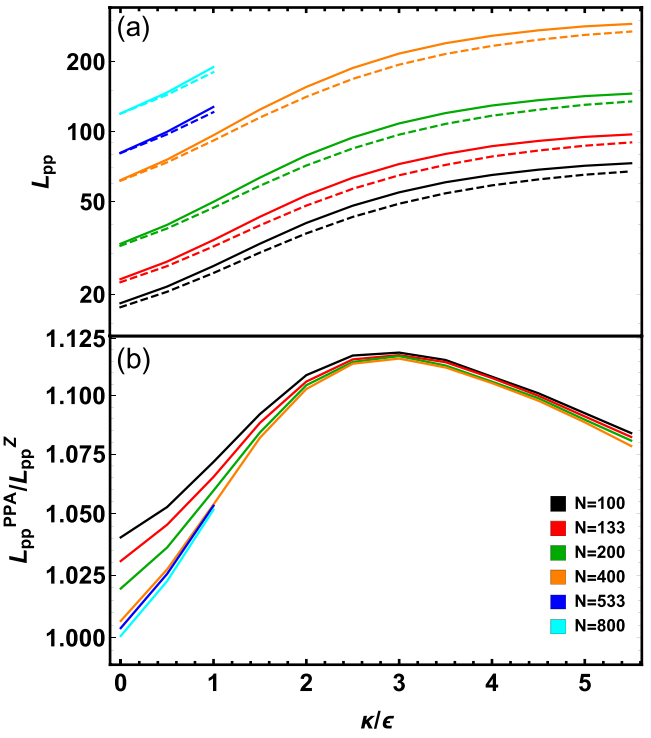

Figure 1. TA-method dependence of L_{pp}. (a) $L_{pp}(\kappa)$ for all chain lengths employed in this study. Solid (dashed) curves show PPA (Z1+) values of L_{pp}. (b) Ratios $L_{pp}^{PPA}(\kappa)/L_{pp}^{Z1+}(\kappa)$ for all N.

Next we explore the differences between estimates of N_e^{rheo} and N_e^{topo} in detail. Two of us recently showed[46] that extrapolating the Svaneborg−Everaers estimator (eq 17) to the $N \to \infty$ limit by fitting PPA data for $L_{pp}(\kappa)$ for all $0 \le \kappa \le 5.5\epsilon$ and $100 \le N \le 800$ is captured by the equation

$$\mathcal{N}_e^{SE}(\kappa, N) = N_e^{rheo}(\kappa) - \frac{b(\kappa)}{N} \tag{19}$$

where N_e^{rheo} and b are κ-dependent fitting parameters. This yields[46]

$$N_e^{rheo}(\kappa) = 80.5 - 70.4 \tanh\left(\frac{\kappa}{1.579\epsilon}\right) \tag{20}$$

Note that fractional differences between $N_e^{rheo}(\kappa)$ and $\mathcal{N}_e^{SE}(\kappa, N)$ were as high as 10% for N as large as 400.

Figure 2a shows $\langle Z \rangle$ for all systems, i.e., for all κ and N. We find that Z1+ yields $\langle Z \rangle$ that are linear in N over the entire

https://doi.org/10.1021/acs.macromol.1c02597
Macromolecules 2022, 55, 3613−3626

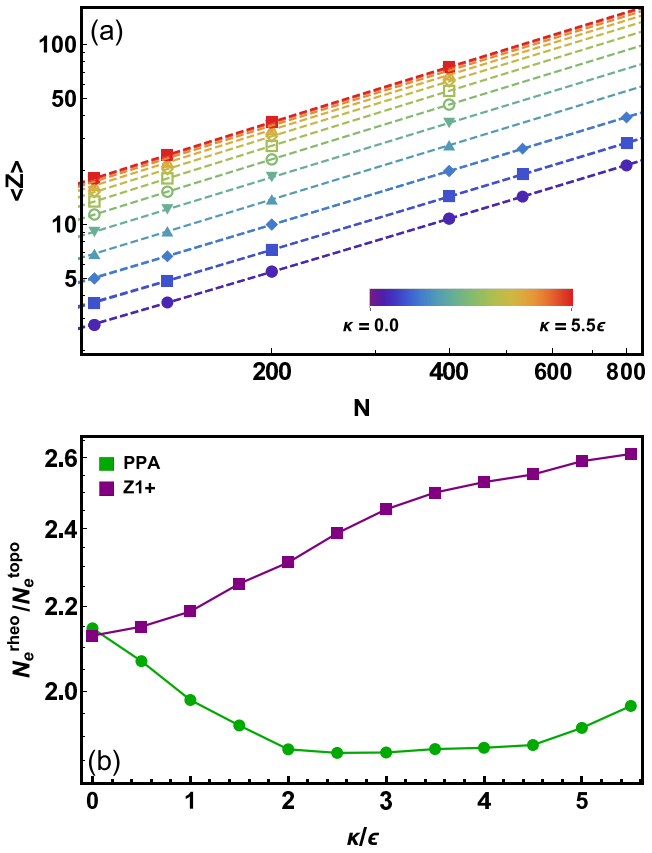

Figure 2. Z1+ results for entanglement and their relation to PPA results. (a) Plot of $\langle Z \rangle$ vs N for all the different κ employed here. Dashed lines are linear fits; their slopes $d\langle Z \rangle/dN$ determine N_e^{topo} (eq 16) because the asymptotic $\langle Z \rangle \propto N$ regime (eq 15) has already been reached at $N = 100$. (b) Method dependence of the ratios $N_e^{rheo}(\kappa)/N_e^{topo}(\kappa)$. The green and purple symbols respectively indicate $N_e^{rheo}(\kappa)$ values extrapolated from eq 19 by using PPA and Z1+ values of L_{pp}.

range $100 \leq N \leq 800$ for all κ. Fitting the inverse slopes $(d\langle Z \rangle/dN)^{-1}$ to a function of the same form as eq 20 yields

$$N_e^{topo}(\kappa) = 37.6 - 32.4 \tanh\left(\frac{\kappa}{1.72\epsilon}\right) \tag{21}$$

Comparing the N_e^{topo} data to the N_e^{rheo} data yields an additional insight about the TA-method dependence. As shown in Figure 2b, if PPA values of $L_{pp}(N)$ are used to estimate $N_e^{rheo}(\kappa)$ (via eq 19), the ratio $N_e^{rheo}(\kappa)/N_e^{topo}(\kappa)$ decreases from ~2.14 for $\kappa = 0$ to ~1.82 for $2\epsilon \leq \kappa \leq \epsilon$ before increasing again to ~1.95 by $\kappa = 5.5\epsilon$. These values deviate from Everaers' prediction[50] $N_e^{rheo}/N_e^{topo} = 2$ by <10% over the entire range of κ. On the other hand, if Z1+ values of $L_{pp}(N)$ are used to estimate $N_e^{rheo}(\kappa)$ (via eq 19), the agreement with Everaers' prediction is much poorer; the ratio $N_e^{rheo}(\kappa)/N_e^{topo}(\kappa)$ increases from ~2.13 to ~2.61 over the range $0 \leq \kappa \leq 5.5\epsilon$.

The ratio N_e^{rheo}/N_e^{topo} is believed to be closely related to entanglement spatial fluctuations, including the fact that the distributions $P(n_e)$ of chemical distances between consecutive entanglements along chains are not δ-distribution-like $[P(n_e) = \delta(n_e - N_e)]$ but instead are Poisson-distributed with a width comparable to N_e.[51,57,58] Such fluctuations have rheological consequences, up to and including altering the prefactor of the $G_N^0 \propto \rho k_B T N_e^{-1}$ relation.[53,59] This prefactor is also predicted by some theories to increase with chain stiffness as energetic contributions from chain bending become important.[22,60] It would be very interesting to examine the trends in $N_e^{rheo}(\kappa)/N_e^{topo}(\kappa)$ in greater detail and relate them to trends in $P(n_e)$, which has, to the best of our knowledge, not yet been investigated for semiflexible bead–spring melts. Doing so, however, is beyond the scope of this study. Throughout the remainder of this paper, we will employ only PPA values of $L_{pp}(\kappa)$. We will show in section 3.4 that this choice produces good agreement with experiments.

Despite the substantial quantitative differences between them, the $N_e^{rheo}(\kappa)$ and $N_e^{topo}(\kappa)$ data, and hence eqs 20 and 21, are qualitatively very similar as illustrated in Figure 3. In

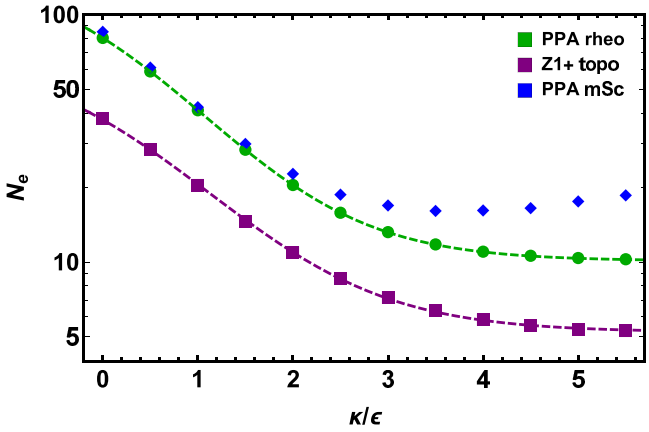

Figure 3. Comparison of N_e estimates calculated by using different methods. The dashed curves show that eqs 20 and 21 quantitatively capture all trends in N_e^{rheo} and N_e^{topo}.

particular, they both exhibit a clear plateau for $4\epsilon \lesssim \kappa \lesssim 5.5\epsilon$. This plateau matches the one previously reported by Bobbili and Milner for model concatenated ring-polymer melts.[61] It corresponds to the semiflexible regime (identified by Milner[33]) where entanglement is maximal and Edwards–de Gennes ($\mu = 2$) scaling is expected to hold. In this regime, entangled strands roughly coincide with Kuhn segments. As chain stiffness continues to increase, local nematic order develops and $N_e(\kappa)$ increases,[34] marking the end of the regime where theories like those of refs 20–25 and 32–34 (all of which assume systems are isotropic) can be expected to hold. This semiquantitative agreement of N_e-estimates obtained in very different ways strongly suggests that the functional form of eqs 7–9 is robust.

However, Figure 3 also shows that some widely used N_e-estimators produce qualitatively different and misleading trends for semiflexible chains. For example, results for the modified S-coil-estimator[37]

$$N_e^{mSc} = (N-1)\left(\frac{\langle L_{pp}^2 \rangle}{\langle R_{ee}^2 \rangle} - 1\right)^{-1} \tag{22}$$

where $\langle R_{ee}^2 \rangle$ is chains' average squared end-to-end distance, lack the above-mentioned plateau, instead passing through a clear minimum at $\kappa \simeq 4\epsilon$ before increasing over the range $4\epsilon \lesssim \kappa \leq 5.5\epsilon$. This qualitative difference arises directly from the fact that eq 22 does not account for non-Gaussian primitive path

https://doi.org/10.1021/acs.macromol.1c02597
Macromolecules 2022, 55, 3613–3626

Table 2. Parameter Values for Eqs 7−10 Obtained by Fitting PPA Values of N_e to Eq 10 Using Two Different Methods[a]

method	α	β	γ	c_1	c_2	c_3
1	443 ± 6	14.2 ± 1.1	5.30 ± 0.09	257 ± 3	10.8 ± 0.8	4.75 ± 0.08
2	512 ± 13	0	6.48 ± 0.13	297 ± 7	0	5.81 ± 0.12

[a]The three-parameter method 1 has unconstrained (α, β, γ), while two-parameter method 2 imposes the constraint $\beta = 0$. The fractional uncertainties on c_1, c_2, and c_3 are the same as the fractional uncertainties on α, β, and γ for each method.

statistics. Because its implicit assumption that primitive paths are random-walk-like between consecutive entanglement points (i.e., that $L_e \gg l_K$) breaks down as chains become semiflexible, the increase in $N_e^{\mathrm{mSc}}(\kappa)$ is spurious.

Taken together, the above results indicate that while expressions like eqs 5−9 are robust against changing the method used to estimate N_e, "external" criteria such as the prediction $N_e^{\mathrm{rheo}}/N_e^{\mathrm{topo}} = 2$ are required to determine which method yields the c-coefficients that will best match experimental data. Another such criterion is the observation that N_e^{rheo} values better correspond to the N_e inferred from rheological measurements of $G = 4\rho k_B T/5N_e$.[50,62] Because we wish to obtain c-coefficients that predict the experimentally measured GI_K^3/k_BT for polymer melts of a given Λ, we will use PPA values of N_e^{rheo} corresponding to the green curves and symbols in Figure 3 as our N_e estimates in all analyses presented below.[e]

3.2. How to Obtain l_K and Λ. Next we performed an unconstrained least-squares fit[f] of $\ln(N_e/C_\infty)$ to $\ln(\alpha C_\infty^{-4} + \beta C_\infty^{-2} + \gamma C_\infty^{-2\epsilon})$ with $\epsilon = 2/5$, where C_∞ was obtained as described below. In other words, we followed the same procedure employed in ref 34, but with $\epsilon = 2/5$ rather than $\epsilon = 1/3$. This change was made to achieve better agreement with the experimental stiff-chain results discussed below. Motivated by multiple discussions with colleagues and new experimental data,[28] we also performed the same type of fit with the constraint $\beta = 0$. These fits respectively yielded the "method 1" and "method 2" values given in Table 2. For both methods, $c_1 = \alpha(\rho l_0^3)^2$, $c_2 = \beta(\rho l_0^3)$, and $c_3 = \gamma(\rho l_0^3)^{2/5}$.

Figure 4 compares bead−spring data for N_e/C_∞ and $4\rho l_0^3 C_\infty^2/5N_e$ to the corresponding analytic expressions for L_e/l_K and GI_K^3/k_BT, i.e., to eqs 7 and 9, for both fit methods. Figure 4a shows that the three-parameter method 1 fit is clearly better, but only slightly so, raising the question of whether the slightly better fit justifies the inclusion of the third fitting parameter (i.e., c_2, which accounts for the contributions of $\mu = 2$ entanglement). In fact, the method 1 and method 2 expressions for GI_K^3/k_BT (Figure 4b) are nearly indistinguishable on the scale of the plot.

While the statistical uncertainties on N_{eK} are very small (~0.1%) owing to our large data sets, uncertainties on C_∞ are larger because of the ambiguities inherent to estimating it. Here we estimated $C_\infty \equiv l_K/l_0$ by fitting the chain statistics to the continuous wormlike-chain model:

$$\frac{\langle R^2(n)\rangle}{nl_0^2} = C_\infty\left\{1 - \frac{C_\infty}{2n}\left[1 - \exp\left(-\frac{2n}{C_\infty}\right)\right]\right\} \tag{23}$$

where $\langle R^2(n)\rangle$ is the mean-squared distance between monomers separated by chemical distance n. Results are somewhat sensitive to the range of n employed in the fits, and

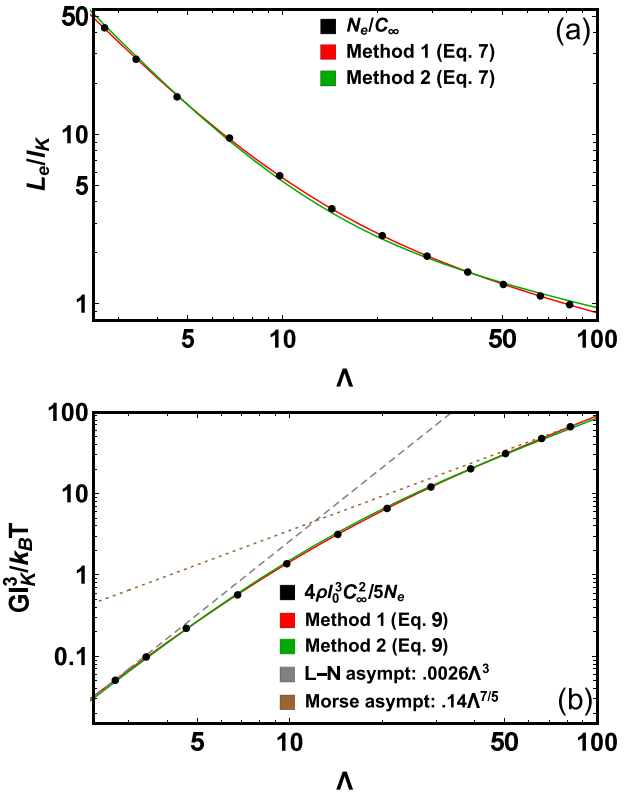

Figure 4. Comparison of bead−spring data for the reduced entanglement length and plateau modulus to the corresponding analytic expressions (eqs 7 and 9) with the c coefficients given in Table 2. The dashed lines indicating Lin−Noolandi and Morse scaling in the asymptotic small-Λ and large-Λ limits are guides to the eye.

alternative methods such as fitting to the discrete wormlike-chain formula (Appendix A)

$$\frac{\langle R^2(n)\rangle}{nl_0^2} = C_\infty - \frac{C_\infty^2 - 1}{2n}\left[1 - \left(\frac{C_\infty - 1}{C_\infty + 1}\right)^n\right] \tag{24}$$

also give slightly different C_∞. These effects produce corresponding uncertainties in Λ and N_e. We believe that both curves in Figure 4b lie within the associated statistical uncertainties. Moreover, comparison of the bead−spring data for GI_K^3/k_BT to $\mu = 7/5$ scaling (i.e., to the brown dashed curve in Figure 4b) indicates that our stiffer chains ($\kappa \geq 5\epsilon$) are approaching the asymptotic Morse-scaling regime, further suggesting that the $\mu = 2$ terms may not be necessary. However, since the above arguments are suggestive rather than conclusive, we defer judgment on this issue to section 3.4.

3.3. Rationale for the Three-Parameter Model. One of the fundamental ideas underlying $\mu = 3$ scaling is the Lin−Noolandi conjecture $a \propto p$.[20,21] This conjecture is well-supported by experiments, which have shown $a \simeq 20p$ for synthetic commodity polymers.[63] Multiplying eq 8 by Λ yields a generalized Lin−Noolandi relation:

https://doi.org/10.1021/acs.macromol.1c02597
Macromolecules 2022, 55, 3613−3626

$$\frac{a}{p} = \sqrt{c_1 + c_2\Lambda + c_3\Lambda^{8/5}} \tag{25}$$

Multiplying eq 8 by $l_K/l_0 \equiv C_\infty \equiv (\rho l_0^3)^{-1/2}\Lambda^{1/2}$ yields an expression for another reduced tube diameter:

$$\frac{a}{l_0} = \frac{1}{\sqrt{\rho l_0^3}}[c_1\Lambda^{-1} + c_2 + c_3\Lambda^{3/5}]^{1/2} \tag{26}$$

The $(\rho l_0^3)^{-1/2}$ term in eq 26 makes it chemistry-dependent. However, because $(\rho l_0^3)^{1/2} = \lambda^{1/2} l_0$, multiplying it by $\lambda^{1/2} l_0$ yields the chemistry-independent expression

$$\lambda^{1/2} a = [c_1\Lambda^{-1} + c_2 + c_3\Lambda^{3/5}]^{1/2} \tag{27}$$

Because λ^{-1} is one measure of chains' effective cross-sectional area,[14,33] λa^2 is simply the ratio of the cross-sectional areas of tubes and individual chains.

Bead−spring data for a/p and $\lambda^{1/2}a$ can be extracted from PPA results as follows. Using the commonly employed definitions $a = (L_e l_K)^{1/2} = (N_e l_0^2 C_\infty)^{1/2}$ and $p = N(\rho\langle R_{ee}^2\rangle)-1 = (\rho l_0 l_K)^{-1} = (\rho l_0^2 C_\infty)^{-1}$,[15,21] one obtains $a/p = \rho l_0^3 C_\infty^{3/2} N_e^{1/2}$ and $\lambda^{1/2}a = \pi\rho l_0^3 (C_\infty N_e)^{1/2}$. Figure 5 compares this data to the corresponding analytic expressions (eqs 25 and 27) for both fitting methods. As shown in Figure 5a, both the data and the analytic expressions for a/p increase from ∼17.5 to ∼23 over the range $2.5 \le \Lambda \le 10$ corresponding to flexible synthetic polymer melts. Thus, both the data and our analytic expressions agree with the Lin−Noolandi conjecture in this Λ range. Remarkably, the method 1 prediction for the bottom of this range $[a(\Lambda = 2.5) = 17.5p]$ agrees nearly exactly with the result quoted in Fetters et al.'s seminal study.[15]

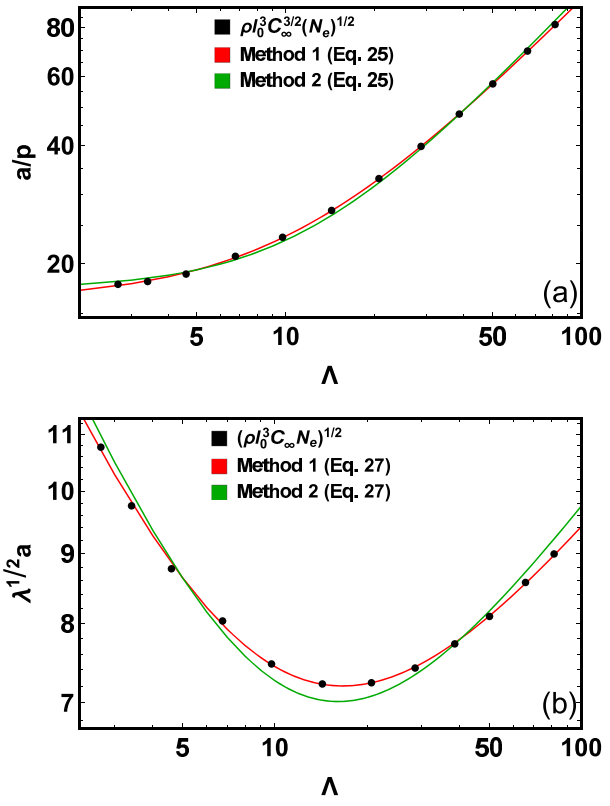

Figure 5. Comparison of bead−spring data for the reduced tube diameters $a/p \equiv \rho l_0 C_\infty^{3/2}(N_e)^{1/2}$ and $\lambda^{1/2}a \equiv \rho l_0^3 (C_\infty N_e)^{1/2}$ to the corresponding analytic expressions (eqs 25 and 27) with the c coefficients given in Table 2.

For larger Λ, an increase in a/p is predicted, but one must be wary of the fact that the scaling definition of the packing length $[p = (\rho l_0 l_K)^{-1}]$ drops far below the chain diameter σ, which is perhaps physically unreasonable.[33,64] At this point it is worth mentioning that none of the results presented above or below *require* employing the packing length. Of the four definitions of Λ given in eq 2, l_K/p [with p calculated using its scaling definition $p = (\rho l_0 l_K)^{-1}$] has been employed most often in the literature for historical reasons.[15−17] Fortunately, its three other definitions $\Lambda \equiv \lambda l_K^2 = \rho_K l_K^3 = l_K^3/v_K$ do not suffer from comparable physical plausibility issues. Indeed, since $l_0 l_K = b^2$ where b is the chains' statistical segment length, the Lin−Noolandi conjecture can also be written as $a \propto (\rho b^2)^{-1}$, and a/p in eq 25 and Figure 5 can be replaced by $\rho b^2 a$. Doing so recasts the Lin−Noolandi conjecture in terms of *intrachain* structure.

Figure 5b illustrates a feature that distinguishes the two- and three-parameter versions of our unified theory (eqs 7−9, 25, and 27) better than any of the above-mentioned results. Because l_0 and $\lambda = \rho l_0 = 0.82$ are essentially constant in our simulations, $\lambda^{1/2}a$ tracks a, and its minimum in the range $15 \lesssim \Lambda \lesssim 20$ matches a corresponding minimum in the tube diameter. Intriguingly, this minimum also corresponds to maximal dominance of the $\mu = 2$ terms in these equations. Accordingly, the method 1 version of eq 27 quantitatively captures the minimum, whereas the method 2 version does not. As discussed above, Milner has identified[33] $\mu = 2$ scaling with a Λ-regime where entangled strands coincide with Kuhn segments. Our results suggest that the center of this regime coincides with a minimum in the ratio of the cross-sectional areas of tubes and individual chains. That this ratio should be minimized when entangled strands coincide with Kuhn segments is expected, but it had not previously been shown; one might argue that our result provides an additional microscopic foundation for $\mu = 2$ scaling.

On the other hand, since (i) a is challenging to measure directly in experiments,[65−69] (ii) it remains unclear how well the definition $a \equiv (L_e l_K)^{1/2}$ describes the transverse confinement of semiflexible chains,[g] and (iii) the method 1 and method 2 versions of our expressions have so far agreed semiquantitatively for all quantities other than $\lambda^{1/2}a$, we continue to defer judgment as to which version is optimal. In the following section, we will attempt to resolve this issue by comparing both versions of eq 9 to *experimental* plateau moduli.

3.4. Comparison to Experiments.

Uchida et al.'s crossover expression for GI_K^3/k_BT (eq 6) was obtained by using a combination of scaling arguments, bead−spring simulation data, experimental results for flexible synthetic polymer melts[15−17] with $2 \lesssim \Lambda \lesssim 11$, and experimental data for stiff biopolymeric solutions[18,19] with $3 \times 10^3 < \Lambda \lesssim 2 \times 10^5$. Until very recently, no experimental data for systems in the range $12 < \Lambda < 3 \times 10^3$ were available. Fortunately, Fenton et al. have just characterized[28] the rheological properties of 12 semiflexible (conjugated and/or aromatic) polymers, 9 of which have $12 < \Lambda \le 320$. On the basis of this new data as well as the above-mentioned experimental results, they proposed a unified expression for the reduced plateau modulus:[28]

https://doi.org/10.1021/acs.macromol.1c02597
Macromolecules 2022, 55, 3613−3626

$$\frac{GI_K^3}{k_BT} = \frac{4}{5}[320\Lambda^{-3} + 6.22\Lambda^{-7/5}]^{-1} \quad (28)$$

This expression is equivalent to our method 2 expression

$$\frac{GI_K^3}{k_BT} = \frac{4}{5}[297\Lambda^{-3} + 5.81\Lambda^{-7/5}]^{-1} \quad (29)$$

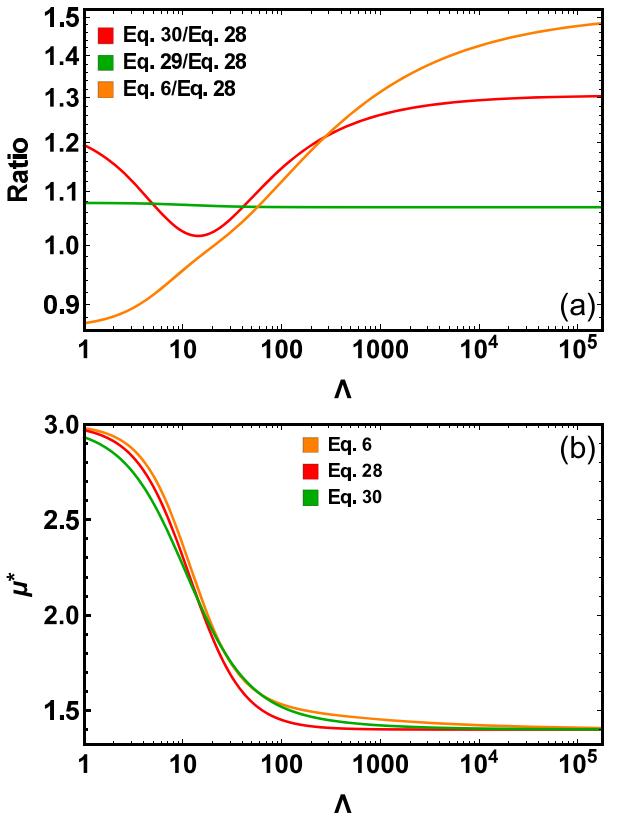

Figure 6. Comparison of the various unified expressions for GI_K^3/k_BT: (a) Λ-dependent ratios of the formulas; (b) their local scaling exponents $\mu^*(\Lambda)$ obtained by using eq 31.

apart from having slightly larger c coefficients. Specifically, as shown in Figure 6a, eq 29 exceeds eq 28 by a nearly constant 7−8% and remains within 30% of our method 1 expression

$$\frac{GI_K^3}{k_BT} = \frac{4}{5}[257\Lambda^{-3} + 10.8\Lambda^{-2} + 4.75\Lambda^{-7/5}]^{-1} \quad (30)$$

over the entire range of Λ ($2 \lesssim \Lambda \lesssim 2 \times 10^5$) for which experimental data are available. In contrast, eq 6 increases monotonically from ∼88% to ∼149% of eq 28 over this range.

The differences between eqs 6 and 28−30 can be better understood and placed in context with previous scaling theories by examining the "local" scaling exponent[34]

$$\mu^*(\Lambda) = \frac{d\ \ln[GI_K^3/k_BT]}{\mathrm{d}[\ln(\Lambda)]} \quad (31)$$

Large $|\mathrm{d}\mu^*/\mathrm{d}\Lambda|$ correspond to crossovers from one type of scaling to another. For example, Lin−Noolandi, Edwards−de Gennes, and Morse scaling respectively have Λ-independent $\mu^* = 3$, 2, and 7/5, and Milner's unified geometrical picture of entanglement[33] predicts sharp crossovers between them, i.e., δ-function-like $|\mathrm{d}\mu^*/\mathrm{d}\Lambda|$ at the crossover Λ.

Figure 6b plots the $\mu^*(\Lambda)$ associated with the various unified formulas. Because the ratio of eq 29 to eq 28 is nearly constant, their $\mu^*(\Lambda)$ values are effectively identical. Relative to these expressions (recall that the c-coefficients in eq 28 were determined entirely by fitting experimental data[15−19,28]), eq 30 has a lower μ^* for $\Lambda \ll 10$. In other words, unlike the other expressions, it predicts $\mu^* \simeq 2.8$ at the bottom of the experimentally relevant Λ-range. On the other hand, both eq 30 and (especially) eq 6 predict a slower crossover to the asymptotic $\lim_{\Lambda\to\infty} \mu^*(\Lambda) = 7/5$ scaling. However, not wishing to take eq 28 as gospel, we continue our analyses by comparing these expressions directly to experimental data for specific polymers. Eqs 6, 28, and 30 are compared to the available experimental data in Figure 7.

Figure 7a shows that all three equations agree semi-quantitatively with experiment for systems spanning 5 orders of magnitude in Λ. The flexible-melt regime ($2 \lesssim \Lambda \lesssim 11$) is populated by a wide variety of commodity synthetic polymers including polyolefins, polydienes, and polyacrylics. Compared to all of the unified theoretical expressions, the experimental data follow $\mu^* = 3$ scaling (i.e., are accurately described by the packing model) up to larger Λ. However, some of the apparent disagreement may arise from a single measurement; the outlying data point at $\Lambda = 11$ correspond to a polyethylene (PE) sample characterized at a temperature below its T_{melt} that may have possessed some local crystalline order.[63]

The agreement of these theoretical expressions with experimental data for stiff biopolymers (which have $\Lambda > 3 \times 10^3$) is similarly good. The experimental data generally follow Morse scaling and are well fit by $GI_K^3/k_BT = 0.157\Lambda^{7/5}$. The large-Λ limits of the crossover expressions are $0.128\Lambda^{7/5}$ (eq 28), $0.138\Lambda^{7/5}$ (eq 29), $0.168\Lambda^{7/5}$ (eq 30), and $0.195\Lambda^{7/5}$ (eq 6). Remarkably, eq 30 achieves the best agreement even though it was obtained by using only bead−spring simulation data for systems with $\Lambda \lesssim 81$.

For the intermediate-Λ ($25 \lesssim \lambda \lesssim 320$) regime populated by the majority of Fenton et al.'s conjugated-polymer melts,[28] all the unified expressions match the two lowest-Λ melts' GI_K^3/k_BT to within <5% and overpredict the GI_K^3/k_BT of the larger-Λ non-nematic melts[h] by 30−60%. Note that experimentally measuring l_K (and hence estimating Λ) for these systems is challenging for several reasons, e.g., low-yield synthesis procedures and high melting temperatures.[28,72]

Figure 7b quantitatively compares the various expressions to the experimental data; the ratio shown is

$$\frac{(GI_K^3/k_BT)_{th}}{(GI_K^3/k_BT)_{exp}} \quad (32)$$

where "th" denotes eqs 6, 28, or 30 and "exp" denotes an experimental data point for the given value of Λ. Equation 30 agrees with experiment to within a factor of 2 for all systems, while eqs 28 and 6 agree with experiment to within a factor of 2 for all but one and three systems, respectively. The mean and root-mean-square (RMS) fractional deviations of the predictions from experiment for each expression are shown in Table 3. Equation 28 has the smallest RMS deviation but the largest mean deviation. In contrast, eq 30 has a slightly larger RMS deviation but a much smaller mean deviation. Moreover,

https://doi.org/10.1021/acs.macromol.1c02597
Macromolecules 2022, 55, 3613−3626

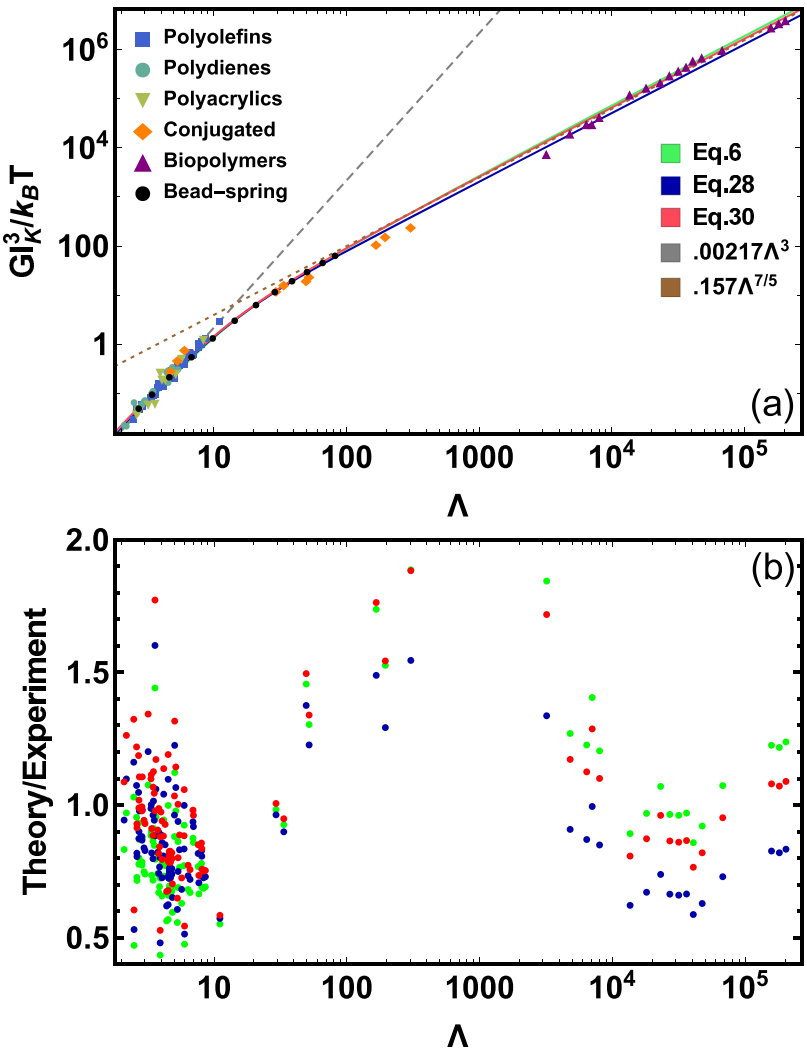

Figure 7. (a) Comparison of theoretical expressions for GI_K^3/k_BT to experimental results for flexible synthetic polymers,[15−17] semiflexible conjugated polymers,[28] and stiff biopolymers.[18,19] Solid curves show the various unified analytic formulas discussed in the text, while the dashed and dotted lines respectively show fits of Lin−Noolandi and Morse scaling to the low-Λ and high-Λ experimental data. Bead−spring data for $4\rho I_0^3 C_\infty^2/5N_e^\infty$ are also shown. (b) Ratios of the various theoretical predictions to experimental data for the same value of Λ. The comparison to eq 29 is not shown here because it precisely tracks the comparison to eq 28. Fractional uncertainties on the experimental G are of order 10% (cf. section 4); the uncertainties on the measured l_K and hence on the experimental GI_K^3/k_BT and Λ may be substantially larger.[28,63,71]

Table 3. Statistics of the Fractional Deviations from Experiment for the Various Unified Expressions for $GI_K{}^3/k_BT$ (All Values in %)[a]

type	eq 6	eq 28	eq 29	eq 30
mean	−12.6	−13.4	−7.0	2.3
RMS	27.2	21.0	22.5	25.3

[a]The table provides both the mean and root-mean-square (RMS) deviations. If one doubles all the c coefficients from our previous work[34] in eq 9 (i.e., assumes $N_e^{\text{theo}} \equiv 2N_e^{\text{topo}}$), the mean and RMS deviations of the resulting expression are −9.1% and 26.7%.

as shown above, it describes bead−spring simulation data better than two-parameter expressions like eqs 28 and 29.

4. CONCLUSIONS

This work attempted to shed light on a topic that has been extensively debated over the past 40 years: the influence of molecular parameters on the plateau modulus of polymer melts. Until very recently, the absence of experimental data in the range $12 < \Lambda < 3 \times 10^3$, where the dimensionless variable $\Lambda \equiv \rho_K l_K^3$ is the scaled Kuhn segment density, presented a barrier to further theoretical progress, but new data for conjugated-polymer melts[28] have filled in much of this gap. Here we demonstrated that the unified analytic model proposed in ref 34 can quantitatively predict the plateau moduli G of flexible, semiflexible, and stiff biopolymeric melts spanning 5 orders of magnitude in Λ and more than 6 orders of magnitude in GI_K^3/k_BT, to a precision comparable to the scatter of the experimental data, provided that sufficient care is devoted to the evaluation of the relevant parameters in the bead−spring melts used to parametrize the model. Our simulation data, obtained by using a coarse-grained model with degrees of polymerization exceeding the entanglement lengths by an order of magnitude, turned out to allow for a precise evaluation of the quantities that characterize entanglement in the $N \to \infty$ limit.

https://doi.org/10.1021/acs.macromol.1c02597
Macromolecules 2022, 55, 3613−3626

We expressed the reduced plateau modulus GI_K^3/k_BT, tube diameter a/l_K, and entanglement length L_e/l_K in terms of Λ and then showed that the functional forms of these unified relations (eqs 7−9) are robust against changing the topological analysis method and the N_e-estimator. By using properly $N \to \infty$ extrapolated PPA values of N_e to obtain the c-coefficients, we obtained a two-parameter expression for GI_K^3/k_BT (eq 29) that agrees quantitatively with the experimental-data-based expression (eq 28) proposed by Fenton et al.;[28] our expression has a slightly smaller mean deviation from the available experimental data points[15−19,28,63] but a slightly larger RMS deviation. While this two-parameter model makes high-quality predictions, we found that the three-parameter version of the model (eq 30) better describes both bead−spring simulation data and the available experimental data, exhibiting a substantially smaller mean deviation and only a slightly larger RMS deviation from experimental data. Thus, we cannot rule out the existence of the $\mu = 2$ scaling regime proposed by Edwards and de Gennes[23,24] and recently discussed in detail by Milner.[33] While both our results and those of ref 28 suggest that it should be of limited relevance in practice, at least for dense melts, more experiments on systems with $10 \le \Lambda \le 30$ are needed to resolve this issue.

Our results have several other implications. First, we find that simulation-based predictions better match experimental results if the bead volume is taken into account during the construction of the entanglement network, even though monomer volume does not explicitly enter the theoretical expressions for reduced entanglement-related quantities (eqs 7−9). A plausible reason for this is that monomer volume is already encoded in the melt density, which suggests that this situation might be different for polymer solutions. Second, consider systems with identical Λ and identical Kuhn lengths l_K but very different microscopic interaction potentials (Appendix A). The present analysis suggests that they should exhibit the same plateau modulus, but this remains to be confirmed. It is plausible that such effects, which alter melts' microstructure but not Λ, account for some of the scatter in the experimental data; tests employing simulations of other coarse-grained or atomistic polymer models could resolve this issue. Third, the agreement between our results and the experimental data for conjugated polymers[28] is striking, suggesting that semiflexible bead−spring polymers are well suited to modeling the rheology of real semiflexible polymers. Fourth, while entanglements hinder relaxation processes, and can be thought of as revealing their nature in measurements that test dynamical properties, our results further support the idea[48,73,74] that entanglement information sufficient to predict polymer melts' primary rheological properties is available from static snapshots. Fifth, the computationally cheapest way to study a polymer melt with $N = zN_e$ over the duration of its terminal relaxation time, where the number of entanglements per chain z is specified by the investigator, can be estimated by using our two- or three-parameter models. This consideration suggests using the bending stiffness $\kappa \simeq 3.2\epsilon$ for simulations conducted at the standard Kremer−Grest melt temperature ($k_BT = \epsilon$);[39] see Appendix B for further details.

Concerning outlook, there are two very computationally expensive tasks for polymer melts with $N \gg N_e$ that could offer additional support for the reported findings in the future: (i) The fact that the same expressions capture data from simulations and experiments implies that they also hold for atomistically detailed models, but this has not yet been verified. (ii) Instead of relating the plateau moduli of bead−spring melts to their measured N_e as described above, they could alternatively be evaluated via rheological measurements.[62] Performing either of these tasks would provide an additional, independent test of our unified analytic expressions. However, substantial care in evaluating the simulated plateau moduli will be necessary to ensure a useful comparison. Estimates of G_N^0 for real polymer melts can vary by ∼10% based on whether G_N^0 is calculated by evaluating the storage modulus $G'(\omega)$ at the frequency ω_{min} which minimizes the loss modulus $G''(\omega)$, terminal peak integration of $G''(\omega)$, the "max" method, or by fitting their time-dependent relaxation modulus $G(t)$ to tube models.[28,71,75] The magnitude and even the sign of fractional differences between the G_N^0 obtained using these different methods and the G_N^0 inferred from TA are likely "chemistry"-dependent and hence will likely be affected by model-specific factors such as the Kremer−Grest model's lower monomer friction and smaller local density fluctuations compared to real or atomistic polymers. Such issues have not yet been investigated in detail.

Finally we emphasize that our unified expressions, which express reduced entanglement-related quantities as a function of the Graessley−Edwards[14] contour length density Λ (and no other variables), apply only to dense melts and concentrated solutions. In particular, since they predict μ^* that increases monotonically with decreasing Λ, they cannot predict the crossover to $\mu = 7/3$ scaling that occurs as the concentration of flexible polymeric liquids is reduced into the semidilute regime.[14,25−27] Our results imply that theories which capture this crossover (in addition to those discussed above) will need to explicitly treat how these reduced quantities vary when the polymer concentration is varied with Λ held fixed.

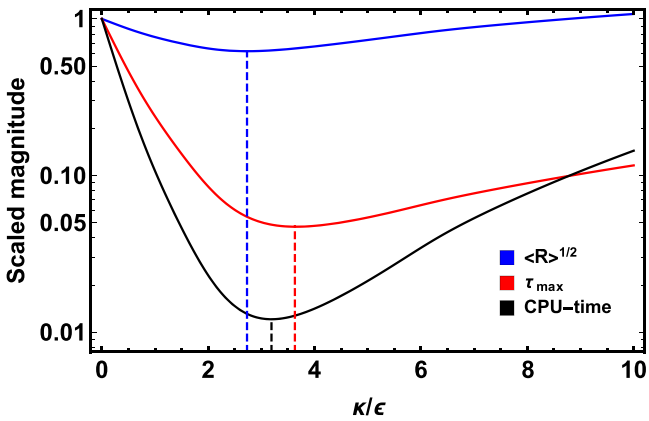

Figure 8. $\langle R_{ee}^2 \rangle^{1/2}$ (blue curve), τ_{max} (red curve), and CPU time (black curve) vs κ/ϵ, relative to values for the flexible system ($\kappa/\epsilon = 0$), for a system with a fixed number of entanglements per chain. Note the semilogarithmic scale. The quantities achieve their minima at κ/ϵ = 2.70, 3.63, and 3.19, respectively, indicated by the dashed lines.

APPENDIX A. KUHN LENGTH AND $\langle R^2 \rangle(n)$ FROM MICROSCOPIC POTENTIALS

As we have expressed the dimensionless plateau modulus in terms of Λ, it might be of further interest to express Λ in terms of the microscopic interaction potentials and k_BT. To accomplish this, we need an expression for the characteristic

https://doi.org/10.1021/acs.macromol.1c02597
Macromolecules 2022, 55, 3613−3626

ratio l_K/l_0 in terms of the microscopic potentials. For chains in melts (and, more generally, ideal chains), the effect of angular bending and torsion potentials $U_{ang}(\theta)$ and $U_{tors}(\phi)$ on l_K can be calculated analytically as follows from the 33-component of the matrix $\mathbf{B} \equiv (\mathbf{1} + \mathbf{A})(\mathbf{1} - \mathbf{A})^{-1}$,[76] i.e.

$$\frac{l_K}{l_0} = C_\infty = [(\mathbf{1} + \mathbf{A})(\mathbf{1} - \mathbf{A})^{-1}]_{33} \tag{33}$$

where the matrix

$$\mathbf{A} = \begin{pmatrix} \langle c_\theta\rangle\langle c_\phi\rangle & \langle c_\theta\rangle\langle s_\phi\rangle & -\langle s_\theta\rangle \\ -\langle s_\phi\rangle & \langle c_\phi\rangle & 0 \\ \langle s_\theta\rangle\langle c_\phi\rangle & \langle s_\theta\rangle\langle s_\phi\rangle & \langle c_\theta\rangle \end{pmatrix} \tag{34}$$

is composed of four different averages that are evaluated via[76]

$$\langle c_\theta\rangle + i\langle s_\theta\rangle = \frac{\int_0^\pi e^{i\theta-\beta U_{ang}(\theta)} \sin(\theta)\, d\theta}{\int_0^\pi e^{-\beta U_{ang}(\theta)} \sin(\theta)\, d\theta} \tag{35}$$

$$\langle c_\phi\rangle + i\langle s_\phi\rangle = \frac{\int_{-\pi}^\pi e^{i\phi-\beta U_{tors}(\phi)}\, d\phi}{\int_{-\pi}^\pi e^{-\beta U_{tors}(\phi)}\, d\phi} \tag{36}$$

with $\beta = 1/k_BT$. For the choice of $U_{ang}(\theta)$ given by eq 13, and in the absence of a torsion potential, eq 33 produces eq 23. For the Kremer–Grest melts studied above, there is a small excluded-volume contribution to the effective bending potential that is only relevant for $\kappa/\epsilon < 2$. It is this regime where the fitting formula (14) clearly outperforms eq 23.

This approach also allows calculation of the bond correlation function, which in turn allows one to write down analytic expressions for all statistical geometrical properties such as the mean-squared end-to-end distance $\langle R^2\rangle(n)$ for a partial chain of chemical length n or the gyration tensor. One obtains[76]

$$\frac{\langle R^2\rangle(n)}{n{l_0}^2} = C_\infty - \frac{2}{n}[\mathbf{A}(\mathbf{1} - \mathbf{A}^n)(\mathbf{1} - \mathbf{A})^{-2}]_{33} \tag{37}$$

with C_∞ already given by eq 33.

When the degree of polymerization is relatively low, rather than employing the continuous wormlike chain model (23), one should employ a discrete wormlike-chain with fixed bond length l_0. In this case, one starts from $U_{ang}(\theta)$ given by eq 13. The matrix $\mathbf{A}$ is then given by eq 34 with the Langevin function $\langle c_\theta\rangle = \mathcal{L} \equiv \coth(\kappa/\epsilon) - (\epsilon/\kappa)$, $\langle s_\theta\rangle = (\pi/2)I_1(k)\,\mathrm{csch}(\kappa/\epsilon)$, and $\langle c_\phi\rangle = \langle s_\phi\rangle = 0$. Equation 37 evaluates to

$$\frac{\langle R^2\rangle(n)}{n{l_0}^2} = C_\infty - \frac{2(1 - \mathcal{L}^n)\mathcal{L}}{(1 - \mathcal{L})^2 n} \tag{38}$$

for the discrete wormlike chain. In eq 38, $C_\infty = (\mathcal{L} - 1)/(\mathcal{L} + 1)$, which can be inverted to read $\mathcal{L} = (C_\infty - 1)/(C_\infty + 1)$, giving rise to eq 24. In this form, the discrete wormlike-chain and freely rotating chain models differ only in the interpretation of C_∞. It can be expressed in terms of κ/ϵ for the former, while the latter's fixed bending angle ϑ implies $\mathcal{L} = \cos(\vartheta)$.

APPENDIX B. CPU TIME

Here, using the results presented above, we estimate the computational effort for studying a semiflexible Kremer–Grest polymer melt with a fixed number z of entanglements per chain, i.e., a degree of polymerization $N \approx zN_e$,[37] for the duration of its terminal relaxation time τ_{max}. While there is some controversy about qualitative and quantitative details,[77] we follow Svaneborg and Everaers[38] and use $\tau_{max} = 3z^3\tau_e$, $\tau_e = \tau_K N_{eK}^2$, and $\tau_K \approx l_K^3\tau_{LJ}\sigma^{-3}$. To avoid finite-size effects, the simulation cell should have a linear size $L_x \sim \sqrt{\langle R_{ee}^2\rangle}$. The number of particles is then $N_{ch}N \sim \rho L_x^3$, and the computing time $\sim N_{ch}N\tau_{max}/\tau_{LJ}$ can be taken as being linear in the number of particles. Plugging in our expressions for $N_e(\kappa)$ and $\langle R_{ee}^2\rangle \approx Nl_0l_K(\kappa)$,[46] τ_{max} has its minimum at $\kappa/\epsilon \approx 3.63$ while the computing time has its minimum at $\kappa/\epsilon \approx 3.19$ for any z. The variation of both quantities with κ is shown in Figure 8.

AUTHOR INFORMATION

Corresponding Author

Robert S. Hoy − *Department of Physics, University of South Florida, Tampa, Florida 33620, United States;* orcid.org/0000-0003-0283-8117; Email: rshoy@usf.edu

Authors

Joseph D. Dietz − *Department of Physics, University of South Florida, Tampa, Florida 33620, United States*

Martin Kröger − *Department of Materials, Polymer Physics, ETH Zürich, CH-8093 Zürich, Switzerland;* orcid.org/0000-0003-1402-6714

Complete contact information is available at: https://pubs.acs.org/10.1021/acs.macromol.1c02597

Notes

The authors declare no competing financial interest.

ACKNOWLEDGMENTS

We are grateful to Abigail Fenton and Ralph H. Colby for numerous helpful discussions and for sharing the experimental conjugated-polymer data[28] shown in Figure 7. This material is based upon work supported by the National Science Foundation under Grant DMR-1555242. M.K. acknowledges support by the Swiss National Science Foundation through Grant 200021L-185052.

ADDITIONAL NOTES

[a]Note that the $\mu = 7/5$ version of Morse's theory implicitly assumes that $a \propto \lambda L_e^3$.

[b]As mentioned in ref 34, our use of the term "contributions" is *not* an indication that the terms in eqs 7–9 proportional to c_1, c_2, and c_3 represent three mechanisms of network elasticity that can act independently; in fact, there is no test that can determine whether a given entanglement is flexible, semiflexible, or stiff.

[c]The heat-bath coupling is achieved by using the LAMMPS Langevin thermostat with damping time $\tau_{Lang} = 10\tau_{LJ}$, and the MD time step employed is $\Delta t = \tau_{LJ}/200$.

[d]For example, the integral part of both Z1 and Z1+ consists of simultaneously considering a pair of adjacent bonds (directed PP segments). In Z1+ the length of both bonds and the orientation of one bond are continuously adjusted. The modification minimizes the sum of the two bond lengths, subject to the constraint that bonds belonging to different chains do not cross each other. In Z1, both bond lengths and

https://doi.org/10.1021/acs.macromol.1c02597
Macromolecules 2022, 55, 3613−3626

orientations are varied simultaneously. Note also that Z1+ is much faster than PPA. On one typical modern CPU core, reducing a melt sample (of the size studied in this paper) to its primitive path mesh takes ∼30 s using Z1+, in contrast to $\sim 10^4$ s using PPA.

[e]Yet another option, by using N_e^{topo} values multiplied by a constant (e.g., 2), is going to be explored elsewhere. See also Table 3.

[f]This logarithmic fit was chosen because it minimizes the mean-squared fractional (rather than the mean-squared absolute) deviation of the MD data from the fitting formula.

[g]Sussman and Schweizer's first-principles microscopic theory of entangled rigid rods,[8,70] which was motivated in part by this issue, is consistent with this definition.

[h]Data for the two melts studied in ref 28 which had GI_K^3/k_BT that fell well below the trendline, presumably because they were partially nematic, are not shown in Figure 7.

REFERENCES

(1) Doi, M.; Edwards, S. F. *The Theory of Polymer Dynamics*; Clarendon Press: Oxford, UK, 1988.

(2) McLeish, T. C. B. Tube theory of entangled polymer dynamics. *Adv. Phys.* **2002**, *51*, 1379.

(3) Graham, R. S.; Likhtman, A. E.; McLeish, T. C. B.; Milner, S. T. Microscopic theory of linear, entangled polymer chains under rapid deformation including chain stretch and convective constraint release. *J. Rheol.* **2003**, *47*, 1171−1200.

(4) Bent, J.; Hutchings, L. R.; Richards, R. W.; Gough, T.; Spares, R.; Coates, P. D.; Grillo, I.; Harlen, O. G.; Read, D. J.; Graham, R. S.; Likhtman, A. E.; Groves, D. J.; Nicholson, T. M.; McLeish, T. C. B. Neutron-mapping polymer flow: Scattering, flow visualization, and molecular theory. *Science* **2003**, *301*, 1691−1695.

(5) Hofmann, M.; Herrmann, A.; Abou Elfadl, A.; Kruk, D.; Wohlfahrt, M.; Rössler, E. A. Glassy, Rouse, and entanglement dynamics as revealed by field cycling 1H NMR relaxometry. *Macromolecules* **2012**, *45*, 2390−2401.

(6) Blanchard, A.; Graham, R. S.; Heinrich, M.; Pyckhout-Hintzen, W.; Richter, D.; Likhtman, A. E.; McLeish, T. C. B.; Read, D. J.; Straube, E.; Kohlbrecher, J. Small angle neutron scattering observation of chain retraction after a large step deformation. *Phys. Rev. Lett.* **2005**, *95*, 166001.

(7) Graham, R. S.; Bent, J.; Hutchings, L. R.; Richards, R. W.; Groves, D. J.; Embery, J.; Nicholson, T. M.; McLeish, T. C. B.; Likhtman, A. E.; Harlen, O. G.; Read, D. J.; Gough, T.; Spares, R.; Coates, P. D.; Grillo, I. Measuring and predicting the dynamics of linear monodisperse entangled polymers in rapid flow through an abrupt contraction. A small angle neutron scattering study. *Macromolecules* **2006**, *39*, 2700−2709.

(8) Sussman, D. M.; Schweizer, K. S. Microscopic Theory of the Tube Confinement Potential for Liquids of Topologically Entangled Rigid Macromolecules. *Phys. Rev. Lett.* **2011**, *107*, 078102.

(9) Sussman, D. M.; Schweizer, K. S. Microscopic Theory of Entangled Polymer Melt Dynamics: Flexible Chains as Primitive-Path Random Walks and Supercoarse Grained Needles. *Phys. Rev. Lett.* **2012**, *109*, 168306.

(10) Xie, S.-J.; Schweizer, K. S. Entangled chain polymer liquids under continuous shear deformation: consequences of a microscopically anharmonic confining tube. *Soft Matt* **2018**, *14*, 7052.

(11) Masubuchi, Y.; Takimoto, J.-I.; Koyama, K.; Ianniruberto, G.; Marrucci, G.; Greco, F. Brownian simulations of a network of reptating primitive chains. *J. Chem. Phys.* **2001**, *115*, 4387.

(12) Schieber, J. D.; Andreev, M.; Prausnitz, J. M.; Doherty, M. F.; Segalman, R. A. Entangled Polymer Dynamics in Equilibrium and Flow Modeled Through Slip Links. *Annu. Rev. Chem. Biomol. Eng.* **2014**, *5*, 367−381.

(13) Becerra, D.; Cordoba, A.; Katzarova, M.; Andreev, M.; Venerus, D. C.; Schieber, J. D. Polymer rheology predictions from first principles using the slip-link model. *J. Rheol.* **2020**, *64*, 1035−1043.

(14) Graessley, W. W.; Edwards, S. F. Entanglement interactions in polymers and the chain contour concentration. *Polymer* **1981**, *22*, 1329.

(15) Fetters, L. J.; Lohse, D. J.; Richter, D.; Witten, T. A.; Zirkel, A. Connection between polymer molecular weight, density, chain dimensions, and melt viscoelastic properties. *Macromolecules* **1994**, *27*, 4639.

(16) Fetters, L. J.; Lohse, D. J.; Graessley, W. W. Chain dimensions and entanglement spacings in dense macromolecular systems. *J. Polym. Sci., Part B* **1999**, *37*, 1023.

(17) Fetters, L. J.; Lohse, D. J.; Milner, S. T.; Graessley, W. W. Packing length influence in linear polymer melts on the entanglement, critical, and reptation molecular weights. *Macromolecules* **1999**, *32*, 6847.

(18) Hinner, B.; Tempel, M.; Sackmann, E.; Kroy, K.; Frey, E. Entanglement, Elasticity, and Viscous Relaxation of Actin Solutions. *Phys. Rev. Lett.* **1998**, *81*, 2614.

(19) Schmidt, F. G.; Hinner, B.; Sackmann, E.; Tang, J. X. Viscoelastic properties of semiflexible filamentous bacteriophage fd. *Phys. Rev. E* **2000**, *62*, 5509.

(20) Lin, Y. H. Number of entanglement strands per cubed tube diameter, a fundamental aspect of topological universality in polymer viscoelastity. *Macromolecules* **1987**, *20*, 3080−3083.

(21) Noolandi, J.; Kavassalis, T. A. New view of entanglements in dense polymer systems. *Phys. Rev. Lett.* **1987**, *59*, 2674−2677.

(22) Morse, D. C. Viscoelasticity of Concentrated Isotropic Solutions of Semiflexible Polymers. 1. Model and Stress Tensor. *Macromolecules* **1998**, *31*, 7030−7043.

(23) Edwards, S. F. Statistical Mechanics of Polymerized Material. *Proc. Phys. Soc.* **1967**, *92*, 9.

(24) de Gennes, P. G. Remarks on entanglements and rubber elasticity. *J. Phys., Lett.* **1974**, *35*, 133−134.

(25) Colby, R. H.; Rubinstein, M.; Viovy, J. L. Chain Entanglement in Polymer Melts and Solutions. *Macromolecules* **1992**, *25*, 996.

(26) Huang, Q.; Hengeller, L.; Alvarez, N. J.; Hassager, O. Bridging the Gap between Polymer Melts and Solutions in Extensional Rheology. *Macromolecules* **2015**, *48*, 4158.

(27) Shahid, T.; Huang, Q.; Oosterlinck, F.; Clasen, C.; van Ruymbeke, E. Dynamic dilution exponent in monodisperse entangled polymer solutions. *Soft. Matter* **2017**, *13*, 269.

(28) Fenton, A. M.; Xie, R.; Aplan, M. P.; Lee, Y.; Gill, M. G.; Fair, R.; Kempe, F.; Sommer, M.; Snyder, C. R.; Gomez, E. D.; Colby, R. H. Predicting the plateau modulus from molecular parameters of conjugated polymers. *ACS Central Sci.* **2022**, *8*, 268.

(29) Hinsch, H.; Wilhelm, J.; Frey, E. Quantitative tube model for semiflexible polymer solutions. *Eur. Phys. J. E* **2007**, *24*, 35−46.

(30) Wilhelm, J.; Frey, E. Elasticity of stiff polymer networks. *Phys. Rev. Lett.* **2003**, *91*, 108103.

(31) Mavrantzas, V. G.; Theodorou, D. N. Atomistic simulation of polymer melt elasticity: Calculation of the free energy of an oriented polymer melt. *Macromolecules* **1998**, *31*, 6310.

(32) Uchida, N.; Grest, G. S.; Everaers, R. Viscoelasticity and primitive path analysis of entangled polymer liquids: From F-actin to polyethylene. *J. Chem. Phys.* **2008**, *128*, 044902.

(33) Milner, S. T. Unified Entanglement Scaling for Flexible, Semiflexible, and Stiff Polymer Melts and Solutions. *Macromolecules* **2020**, *53*, 1314.

(34) Hoy, R. S.; Kröger, M. Unified Analytic Expressions for the Entanglement Length, Tube Diameter, and Plateau Modulus of Polymer Melts. *Phys. Rev. Lett.* **2020**, *124*, 147801.

(35) Kröger, M. Shortest multiple disconnected path for the analysis of entanglements in two- and three-dimensional polymeric systems. *Comput. Phys. Commun.* **2005**, *168*, 209.

(36) Flory, P. J. *Principles of Polymer Chemistry*; Cornell University Press: Ithaca, NY, 1953.

https://doi.org/10.1021/acs.macromol.1c02597
Macromolecules 2022, 55, 3613−3626

(37) Hoy, R. S.; Foteinopoulou, K.; Kröger, M. Topological analysis of polymeric melts: Chain-length effects and fast-converging estimators for entanglement length. *Phys. Rev. E* **2009**, *80*, 031803.
(38) Svaneborg, C.; Everaers, R. Characteristic Time and Length Scales in Melts of Kremer-Grest Bead-Spring Polymers with Wormlike Bending Stiffness. *Macromolecules* **2020**, *53*, 1917.
(39) Kremer, K.; Grest, G. S. Dynamics of entangled linear polymer melts - a molecular dynamics simulation. *J. Chem. Phys.* **1990**, *92*, 5057.
(40) Faller, R.; Kolb, A.; Müller-Plathe, F. Local chain ordering in amorphous polymer melts: influence of chain stiffness. *Phys. Chem. Chem. Phys.* **1999**, *1*, 2071.
(41) Weeks, J. D.; Chandler, D.; Andersen, H. C. Role of repulsive forces in determining equilibrium structure of simple liquids. *J. Chem. Phys.* **1971**, *54*, 5237.
(42) Warner, H. R. Kinetic-theory and rheology of dilute suspensions of finitely extendible dumbbells. *Ind. Eng. Chem. Fundam.* **1972**, *11*, 379.
(43) Kröger, M. Simple models for complex nonequilibrium fluids. *Phys. Rep.* **2004**, *390*, 453−551.
(44) Kröger, M. *Models for Polymeric and Anisotropic Liquids*; Springer: New York, 2005.
(45) Everaers, R.; Karimi-Varzaneh, A.; Fleck, F.; Hojdis, N.; Svaneborg, C. Kremer-Grest Models for Commodity Polymer Melts: Linking Theory, Experiment, and Simulation at the Kuhn Scale. *Macromolecules* **2020**, *53*, 1901.
(46) Dietz, J. D.; Hoy, R. S. Facile equilibration of well-entangled semiflexible bead-spring polymer melts. *J. Chem. Phys.* **2022**, *156*, 014103.
(47) Plimpton, S. Fast parallel algorithms for short-range molecular dynamics. *J. Comput. Phys.* **1995**, *117*, 1.
(48) Everaers, R.; Sukumaran, S. K.; Grest, G. S.; Svaneborg, C.; Sivasubramanian, A.; Kremer, K. Rheology and microscopic topology of entangled polymeric liquids. *Science* **2004**, *303*, 823.
(49) Sukumaran, S. K.; Grest, G. S.; Kremer, K.; Everaers, R. Identifying the Primitive Path Mesh in Entangled Polymer Liquids. *J. Polym. Sci., Part B: Polym. Phys.* **2005**, *43*, 917.
(50) Everaers, R. Topological versus rheological entanglement length in primitive-path analysis protocols, tube models and slip-link models. *Phys. Rev. E* **2012**, *86*, 022801.
(51) Tzoumanekas, C.; Theodorou, D. N. Topological analysis of linear polymer melts: A statistical approach. *Macromolecules* **2006**, *39*, 4592.
(52) Masubuchi, Y.; Ianniruberto, G.; Greco, F.; Marrucci, G. Entanglement molecular weight and frequency response of sliplink networks. *J. Chem. Phys.* **2003**, *119*, 6925−6930.
(53) Schieber, J. D.; Indei, T.; Steenbakkers, R. J. A. Fluctuating entanglements in single-chain mean-field models. *Polymers* **2013**, *5*, 643.
(54) Steenbakkers, R. J. A.; Tzoumanekas, C.; Li, Y.; Liu, W. K.; Kröger, M.; Schieber, J. D. Primitive-path statistics of entangled polymers: mapping multi-chain simulations onto single-chain mean-field models. *New J. Phys.* **2014**, *16*, 015027.
(55) Hoy, R. S.; Grest, G. S. Entanglements of an End-Grafted Polymer Brush in a Polymeric Matrix. *Macromolecules* **2007**, *40*, 8389.
(56) Zhou, Q.; Larson, R. G. Primitive Path Identification and Statistics in Molecular Dynamics Simulations of Entangled Polymer Melts. *Macromolecules* **2005**, *38*, 5761−5765.
(57) Schieber, J. D. Fluctuations in entanglements of polymer liquids. *J. Chem. Phys.* **2003**, *118*, 5162.
(58) Foteinopoulou, K.; Karayiannis, N. C.; Mavrantzas, V. G.; Kröger, M. Primitive path identification and entanglement statistics in polymer melts: Results from direct topological analysis on atomistic polyethylene models. *Macromolecules* **2006**, *39*, 4207−4216.
(59) Steenbakkers, R. J. A.; Tzoumanekas, C.; Li, Y.; Liu, W. K.; Kröger, M.; Schieber, J. D. Primitive-path statistics of entangled polymers: mapping multi-chain simulations onto single-chain mean-field models. *New J. Phys.* **2014**, *16*, 015027.
(60) Zou, W.; Larson, R. G. A mesoscopic simulation method for predicting the rheology of semi-dilute wormlike micellar solutions. *J. Rheol.* **2014**, *58*, 681.
(61) Bobbili, S. V.; Milner, S. T. Simulation Study of Entanglement in Semiflexible Polmer Melts and Solutions. *Macromolecules* **2020**, *53*, 3861.
(62) Hou, J.-X.; Svaneborg, C.; Everaers, R.; Grest, G. S. Stress Relaxation in Entangled Polymer Melts. *Phys. Rev. Lett.* **2010**, *105*, 068301.
(63) Fetters, L. J.; Lohse, D. J.; Colby, R. H. In *Physical Properties of Polymers Handbook*, 2nd ed.; Mark, J. E., Ed.; Springer: New York, 2007; pp 447−454.
(64) Bobbili, S. V.; Milner, S. T. Measuring packing length in simulations for different polymer architectures. *J. Rheol.* **2021**, *65*, 1245.
(65) Arbe, A.; Pomposo, J. A.; Asenjo-Sanz, I.; Bhowmik, D.; Ivanova, O.; Kohlbrecher, J.; Colmenero, J. Single chain dynamic structure factor of linear polymers in an all-polymer nano-composite. *Macromolecules* **2016**, *49*, 2354−2364.
(66) Ruocco, N.; Dahbi, L.; Driva, P.; Hadjichristidis, N.; Allgaier, J.; Radulescu, A.; Sharp, M.; Lindner, P.; Straube, E.; Pyckhout-Hintzen, W.; Richter, D. Microscopic relaxation processes in branched-linear polymer blends by rheo-SANS. *Macromolecules* **2013**, *46*, 9122−9133.
(67) Blanchard, A.; Graham, R. S.; Heinrich, M.; Pyckhout-Hintzen, W.; Richter, D.; Likhtman, A. E.; McLeish, T. C. B.; Read, D. J.; Straube, E.; Kohlbrecher, J. Small angle neutron scattering observation of chain retraction after a large step deformation. *Phys. Rev. Lett.* **2005**, *95*, 166001.
(68) Käs, J.; Strey, H.; Tang, J. X.; Finger, D.; Ezzell, R.; Sackmann, E.; Janmey, P. A. F-actin, a model polymer for semiflexible chains in dilute, semidilute, and liquid crystalline solutions. *Biophys. J.* **1996**, *70*, 609−625.
(69) Ewen, B.; Maschke, U.; Richter, D.; Farago, B. Nutron spin-echo studies on the segmental diffusion behavior in the different chain sections of high-molecular-weight poly(dimethylsiloxane) melts. *Acta Polym.* **1994**, *45*, 143−147.
(70) Sussman, D. M.; Schweizer, K. S. Entangled Rigid Macromolecules under Continuous Startup Shear Deformation: Consequences of a Microscopically Anharmonic Confining Tube. *Macromolecules* **2013**, *46*, 5684−5693.
(71) Liu, C.; He, J.; van Ruymbeke, E.; Keunings, R.; Bailly, C. Evaluation of different methods for the determination of the plateau modulus and the entanglement molecular weight. *Polymer* **2006**, *47*, 4461−4479.
(72) Xie, R.; Weisen, A. R.; Lee, Y.; Aplan, M. A.; Fenton, A. M.; Masucci, A. E.; Kempe, F.; Sommer, M.; Pester, C. W.; Colby, R. H.; Gomez, E. D. Glass transition temperature from the chemical structure of conjugated polymers. *Nat. Commun.* **2020**, *11*, 893.
(73) Rubinstein, M.; Helfand, E. Statistics of the entanglement of polymers - concentration effects. *J. Chem. Phys.* **1985**, *82*, 2477.
(74) Kröger, M.; Voigt, H. On a quantity describing the degree of entanglement in linear polymer systems. *Macromol. Theory Simul.* **1994**, *3*, 639−647.
(75) Ferry, J. D. *Viscoelastic Properties of Polymers*; Wiley: Hoboken, NJ, 1980.
(76) Weismantel, O.; Galata, A. A.; Sadeghi, M.; Kröger, A.; Kröger, M. Efficient generation of self-avoiding, semiflexible rotational isomeric chain ensembles in bulk, in confined geometries, and on surfaces. *Comput. Phys. Commun.* **2022**, *270*, 108176.
(77) Lang, P.; Frey, E. Disentangling entanglements in biopolymer solutions. *Nat. Commun.* **2018**, *9*, 494.

https://doi.org/10.1021/acs.macromol.1c02597
Macromolecules 2022, 55, 3613−3626